Journal of Zhejiang University-SCIENCE A (Applied Physics & Engineering) 2024 25(6):502-515
www.jzus.zju.edu.cn; www.springer.com/journal/11582
E-mail: jzus_a@zju.edu.cn

Research Article

https://doi.org/10.1631/jzus.A2300157

Corrosion behavior and protection mechanism of carbon steel coated with ethylene chlorotrifluoroethylene (ECTFE)

Peihu SHEN[1], Jun WEN[1], Biqin DONG[2], Hedong LI[1], Minjia WANG[1,3]✉

[1]*School of Civil Engineering and Architecture, Zhejiang Sci-Tech University, Hangzhou 310018, China*
[2]*College of Civil and Transportation Engineering, Shenzhen University, Shenzhen 518061, China*
[3]*Zhejiang Research Institute of Chemical Industry Co., Ltd., Hangzhou 310023, China*

Abstract: Ethylene chlorotrifluoroethylene (ECTFE) coating was applied to the surface of carbon steel through electrostatic spraying and low-temperature heat treatment. The morphology and structure of the coating were analyzed using various characterization techniques. The electrochemical data of the coated steel soaked in 3.5% (mass fraction) NaCl solution for 90 d at different periods were also examined. The findings indicate that the outer surface of the coating remains structurally stable before and after soaking. F can diffuse into the steel substrate, facilitating the bonding between the coating and the steel substrate, but the free F also induces a weakening effect on the crystalline structure. Due to the thickness of the coating edge and the susceptibility to infiltration of the corrosive medium, under-film micro-zone corrosion occurs at a slow rate. After soaking for 90 d, the impedance modulus measures approximately 10^4 Ω·cm^2, and the open circuit potential (OCP) is −0.61 V. The self-corrosion current density is 1.13×10^{-6} A/cm^2, resulting in a calculated coating protection rate of 99.29%. In summary, despite edge corrosion occurring, the ECTFE coating provides excellent corrosion protection.

Key words: Coating; Fluorine resin; Edge corrosion; Corrosive behavior; Electrochemical performance

1 Introduction

Carbon steel is the predominant material used in steel structures due to its excellent mechanical and processing properties. However, it is susceptible to corrosion in aggressive environments which brings huge safety hazards and economic losses (Molhi et al., 2021; Sengupta et al., 2021; Zhang et al., 2021; Hsissou et al., 2022b; Yan et al., 2022). Hence, corrosion protection is crucial (Douche et al., 2020; Hsissou et al., 2022a; Steffi et al., 2022b). The primary methods for protecting carbon steel from corrosion include cathodic protection and the use of corrosion inhibitors and anticorrosion coatings (Alibakhshi et al., 2018; Hsissou et al., 2021; Shen et al., 2022; Steffi et al., 2022a). Among these methods, anticorrosion coatings are preferred due to effectiveness of the barrier, wide applicability, and cost effectiveness (Hsissou et al., 2018; Steffi et al., 2021; Wang H et al., 2021). However, such coatings often exhibit imperfections, such as localized thin regions, microcracks, and micropores, which can potentially result in localized corrosion beneath the coating despite its overall integrity. This phenomenon is predominantly observed in organic coatings (Haeri et al., 2022). Fluorine resins are commonly used as organic coatings because of their high temperature resistance, weathering resistance, and anti-fouling properties. These characteristics stem from the strong bonding energy of fluorine-carbon bonds, low surface energy, and stable network structure (Rudnev et al., 2016; Lei et al., 2018). Ethylene chlorotrifluoroethylene (ECTFE) is a distinctive thermoplastic fluorine material with a semi-crystalline structure (Liu et al., 2020). It possesses excellent toughness and resistance to aging and fatigue (Cui et al., 2014), as well as remarkable chlorine-resistant effects (Simone et al., 2012). Currently, ECTFE is mainly used in the fields of dialysis and petrochemicals for efficient oil-water separation, achieving permeation fluxes exceeding 99.9% (Pan et al., 2021). There are few studies on the corrosion behavior and

---

✉ Minjia WANG, coolwangmin@zstu.edu.cn
Hedong LI, https://orcid.org/0000-0002-0911-1976
Minjia WANG, https://orcid.org/0000-0003-2954-9999

Received Mar. 24, 2023; Revision accepted July 31, 2023; Crosschecked Feb. 2, 2024; Online first Apr. 5, 2024

protection mechanism of carbon steel coated with ECTFE.

In this study, an ECTFE coating was prepared on the surface of carbon steel by electrostatic spraying and low-temperature heat treatment, followed by soaking in 3.5% (mass fraction) NaCl solution. The corrosion behavior and protection mechanism of the coated steel were studied in-depth. It is evident that corrosion initiates from the periphery due to the thinness of the coating edge. Even so, the ECTFE coating still exhibits corrosion protection performance. The main objective of this study is to provide an empirical and theoretical foundation for protection against edge corrosion in fluororesin coatings and thereby advance durability technology for steel structures and for the development of anti-corrosion coating materials.

2 Experimental

2.1 Raw materials and coating preparation

The ECTFE powder was supplied by Zhejiang Research Institute of Chemical Industry Co., Ltd., China. The steel (HPB300, Φ220 mm, C: 0.21%, Mn: 0.63%, Si: 0.35%) was procured from Zhejiang Fugang Metal Products Co., Ltd., China. The carbon steel was cut into cylindrical blocks with a height of 150 mm. The edges of the steel blocks were chamfered. The surface was polished with 320# SiC sandpaper for 2 min until completely bright, as shown in Fig. 1. After cleaning and drying, ECTFE powder was uniformly sprayed onto one side of the blocks using an electrostatic spraying gun (COLO-500 STAR, Hangzhou Kafan Machinery Equipment Co., China). The air pressure was controlled at 0.5 MPa, and the output voltage was set to 70 kV. The distance between the gun and the substrate was 150 cm while the spraying time was 5 s. Finally, the sprayed samples were put into a muffle furnace and held at 260 °C for 30 min. The resultant samples were steel blocks coated with a transparent ECTFE coating with an approximate thickness of 200 μm.

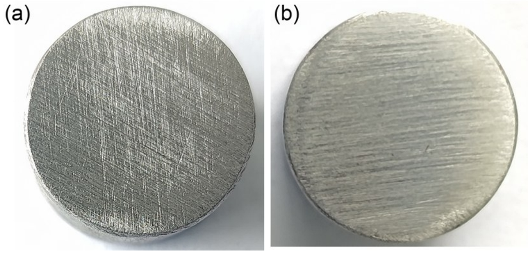

Fig. 1 Images of steel matrix before (a) and after (b) polishing

2.2 Morphological and structural characterization

The heat absorption and exhaustion characteristics of the ECTFE powder were evaluated using a thermal synchrotron analyzer (TG-DSC, STA6000, PerkinElmer, USA) to determine the appropriate heat treatment temperature, with a heating rate of 10 °C/min and temperature range of 30–500 °C. The structural composition of the ECTFE powder, as well as the inner and outer surfaces of the coating, was analyzed using a Fourier transform infrared spectrometer (FT-IR, Nicolet iS20, Thermo Fisher Scientific, USA) in attenuated total reflection (ATR) mode with a wavelength range of 4000–600 cm^{-1}. The phase structure of ECTFE powder together with the inner and outer surfaces of the coating were analyzed by X-ray diffraction (XRD, Ultima IV, Rigaku Corporation, Japan), with a Cu target, tube voltage of 40 kV, tube current of 40 mA, step size of 0.005, wave length λ of 1.5418 Å, scanning speed of 2 (°)/min, and a scanning range of 10°–80°. The microscopic morphology of the ECTFE powder and coating was observed using field emission scanning electron microscopy (SEM, Quanta FEG650, FEI, USA). Additionally, the elemental distribution characteristics at the interface were analyzed with an energy dispersive spectrometer (EDS, EDXA 560, FEI, USA).

2.3 Anti-corrosion and associated performance evaluation

The hydrophilic/hydrophobicity of ECTFE coating before and after soaking was tested using an optical contact angle meter (WCA, JY-82B, Chengde Dingsheng Experimental Machine Checking Equipment Co., Ltd., China). The adhesion of the ECTFE coating was measured before and after soaking according to the standard GB/T 9286–2021 (MOHURD, 2021) at a temperature of 25 °C and a relative humidity of 50%. The uncoated side of the coated steel sample was sealed with thick epoxy resin. The surface edge was also sealed to prevent intrusion of corrosive media towards the uncoated side. The sample was connected with wires at the bottom for electrochemical performance testing, as shown in Fig. 2. Subsequently, the samples were soaked in 3.5% (mass fraction) NaCl solution. An electrochemical workstation (CS2350H, Wuhan Corrtest Instruments Co., Ltd., China) was evaluated to test the

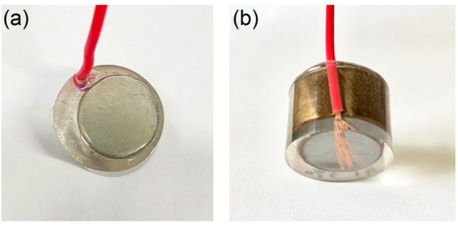

Fig. 2 ECTFE-coated (a) and uncoated (b) sides of the sample

electrochemical performance of the coated steel samples in accordance with the standard GB/T 24196–2009 (MOHURD, 2009). The evaluation included open circuit potential (OCP), electrochemical impedance spectra (EIS), and polarization curves. The electrochemical test was conducted using a standard three-electrode system, with 3.5% (mass fraction) NaCl solution as the electrolyte medium. The working electrode consisted of a series of coated steel samples with an exposed area of approximately 2.5 cm^2, while the reference electrode was a saturated calomel electrode (SCE), and the counter electrode was made of graphite. Additionally, a Luggin capillary was used to minimize the voltage drop. The OCP test required stability for 60 min. The frequency range for EIS testing was 0.01–100 kHz, with an alternating-current (AC) excitation signal amplitude of 10 mV. The dynamic potential scan test was conducted within a voltage range of −500 mV to +500 mV relative to OCP. Considering the influence of error and polarization time, the scan rate was chosen as 0.5 mV/s. The EIS data were analyzed using Zview software. The experiment was initiated at the point, after several hours, when steady-state open circuit potential and corrosion polarization curves were observed. To further test the corrosion resistance of ECTFE coatings, the coated steel samples with cross scratches were subjected to a 720 h salt spray test in a neutral salt spray test chamber in accordance with Kajánek et al. (2009). The size of the salt spray test chamber was 1350 mm× 1150 mm×610 mm. The conditions of the test were 35 °C, 3.5% (mass fraction) NaCl solution, pH=7.0, and pressure of 1 atm (101325 Pa).

3 Results and discussion

3.1 Coating structure and morphology characterization

Fig. 3 shows the TG-DSC curves of ECTFE powder. The TG (thermogravimetry) curve shows a mass loss of approximately 0.82% below 100 °C, attributed to the evaporation of moisture absorbed from the surrounding atmosphere. Beyond 300 °C, a rapid decline in mass is observed, indicating significant degradation and ultimate decomposition of the fluorine resin structure. The endothermic peaks at 215 °C and 300 °C in the DSC (differential scanning calorimetry) curve indicate the melting of powder and breaking of some chemical bonds, respectively. The exothermic peak at 455 °C is ascribed to combustion of organics. It can be inferred that the suitable heat treatment temperature is between 215 and 300 °C. A heat treatment temperature of 260 °C was therefore chosen as the intermediate temperature to ensure that the powder can melt and cross-link compactly without chemical bond breakage.

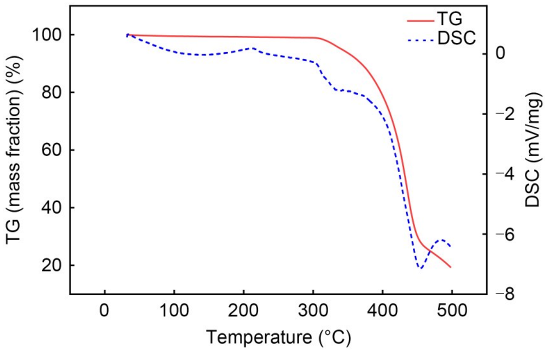

Fig. 3 TG-DSC curves of ECTFE powder

Fig. 4 shows the FT-IR spectra of ECTFE powder, as well as the inner and outer surfaces of the coating before and after soaking in 3.5% (mass fraction) NaCl solution for 90 d. The peaks at 3400 cm^{-1} and 1640 cm^{-1} correspond to the O–H stretching vibrations from water molecules. The peak at 2970 cm^{-1} corresponds to C–H group stretching vibrations. The peaks at 1449 cm^{-1} and 1400 cm^{-1} correspond to the bending vibrations of C–H groups (Ghanbari et al., 2023). The absorption bands in 1400–1100 cm^{-1} are attributed to C–F functional groups, while those in 850–600 cm^{-1} are assigned to C–Cl functional groups (Singh et al., 2012; Abdel-Hady and El-Toony, 2015). The O–H stretching vibration bands originating from water molecules adsorbed onto ECTFE powder surface arise due to atmospheric moisture (Fig. 4a), but they vanish on both inner and outer surfaces after coating formation (Figs. 4d and 4f). By comparing Fig. 4a with others, it can be observed that the positions of spectral lines are essentially identical and thus show the similarity in structure

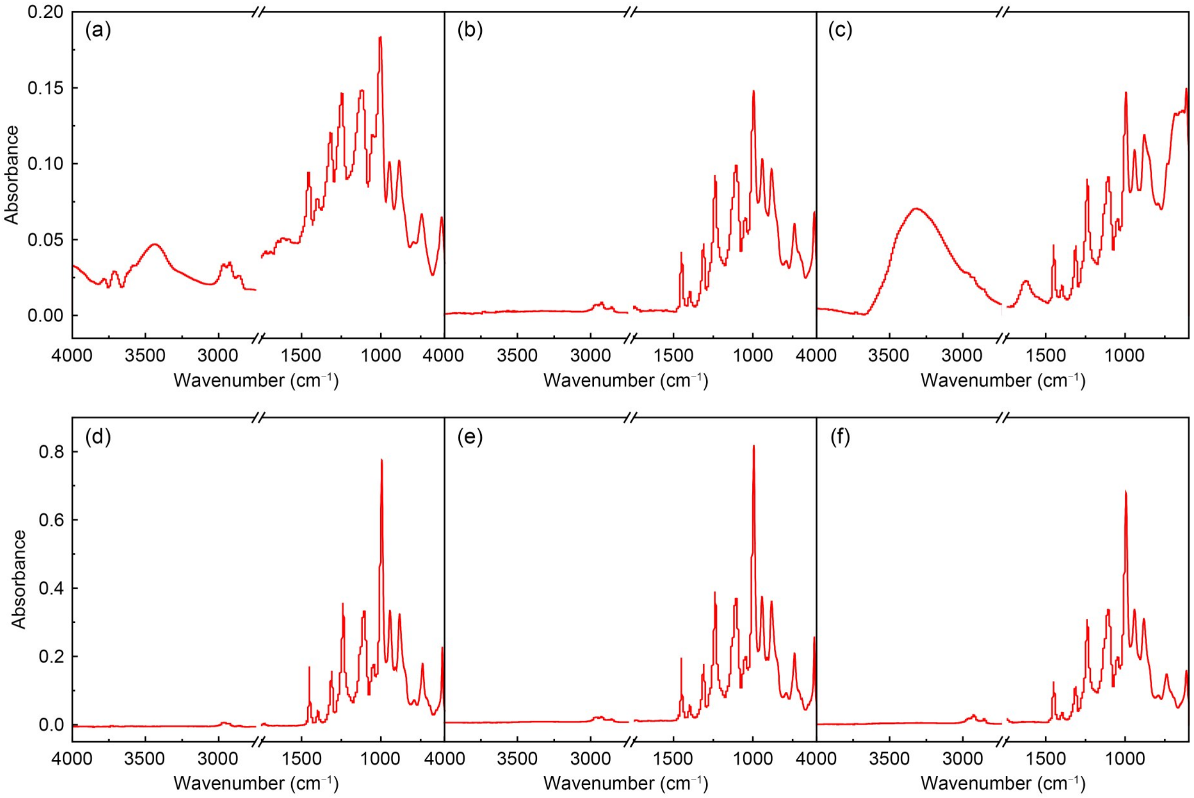

Fig. 4 FT-IR spectra: (a) powder; (b) inner surface of coating center soaking for 90 d; (c) inner surface of coating edge soaking for 90 d; (d) initial outer surface of coating; (e) outer surface of coating soaking for 90 d; (f) initial inner surface of coating

between the powder and the coating. However, there is a significant increase in peak intensity for the coating, indicating an enhancement in dipole moment of chemical bonds as well as an increase in bond polarity and energy (Giannetti, 2005). This ultimately leads to improved structural thermal stability. After soaking for 90 d, no structural changes were observed on the outer surface of the coating (Fig. 4e). However, a significant decrease in peak intensity was detected on the inner surface of the coating center compared to its presoaking state (Fig. 4b). This can be attributed to the negative impact of soaking on interfacial bonding and chemical bonds at the interface. In addition, a prominent peak corresponding to the O-H stretching vibration is observed on the inner surface of the coating edge (Fig. 4c), while the presence of C-Cl functional groups is completely obscured, indicating formation and attachment of products containing crystalline water on the inner surface of the coating edge.

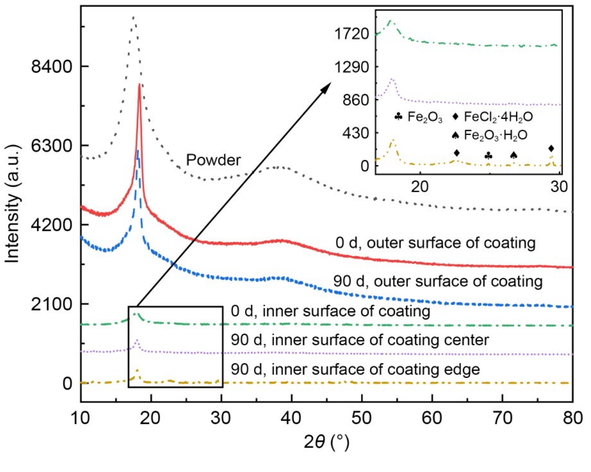

Fig. 5 XRD patterns of ECTFE powder and coating at different periods and parts

Fig. 5 shows the XRD patterns of the ECTFE powder and the inner/outer surfaces of the coating before and after soaking in 3.5% (mass fraction) NaCl solution for 90 d. The broad main peak at 2θ angle of 17.5° and the gentle peak at 2θ angle of 39° are observed in the XRD patterns and indicate that the main phase of both powder and coating is amorphous with semi-crystalline characteristics (Yao et al., 2017). Compared to the powder, the coating exhibits a much sharper main peak and a weaker gentle peak, indicating stronger crystallization compared to the powder. In addition, the inner surface of the coating shows significantly lower intensity for the main peak than for its outer surface. This is probably due to the weakening of crystallinity caused by interfacial bonding between the coating and the steel substrate during heat treatment. After soaking for 90 d, no crystalline impurity phase is observed on the outer surface of the coating. However, a slight decrease in the main peak suggests that the crystallinity of the outer surface of the coating has been weakened. There exist impurity phases on the inner surface of the coating edge, which are $FeCl_2{\cdot}4H_2O$ (JCPDS 71-0688), $Fe_2O_3{\cdot}H_2O$ (JCPDS 03-0440), and Fe_2O_3 (JCPDS 21-0920). They indicate that corrosion has occurred on the inner surface of the coating edge and has resulted in the formation of crystalline water-containing corrosion products. These findings provide a plausible explanation for the observed O–H stretching vibration peak and the masking effect on C–Cl functional groups in the FT-IR spectrum. In addition, the main peak of the inner surface of the coating exhibits a sharper profile and an enhanced intensity after soaking, indicating a strengthened crystallinity. This may be attributed to weakened interfacial bonding between the coating and the steel substrate.

Fig. 6 shows the macroscopic morphological evolution of the coated steel soaked in 3.5% (mass fraction) NaCl solution for different periods. The surface remains free from any visible signs of macroscopic corrosion when observed through the coating. Figs. 7a and 7b show the micromorphology of the ECTFE powder at low and high magnifications, respectively. As shown in Fig. 7a, the ECTFE powder exhibits a micromorphology of irregular flake blocks with an average particle size of 10 μm. These blocks are agglomerated by numerous small spherical particles measuring approximately 20 nm in diameter, as shown in Fig. 7b. The outer surface of the coating remains flat and dense before and after soaking, exhibiting no defects such as holes or cracks, as shown in Figs. 7c and 7d. Figs. 7e and 7g show the cross-sectional morphology of the coating center before soaking at low and high magnifications, respectively, revealing a uniform thickness of

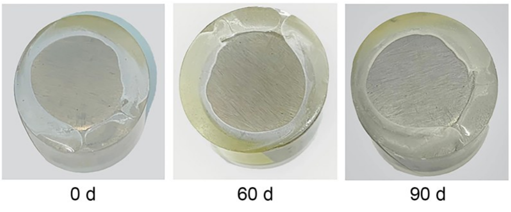

Fig. 6 Macroscopic morphological evolution of coated steel soaking in 3.5% (mass fraction) NaCl solution at different periods

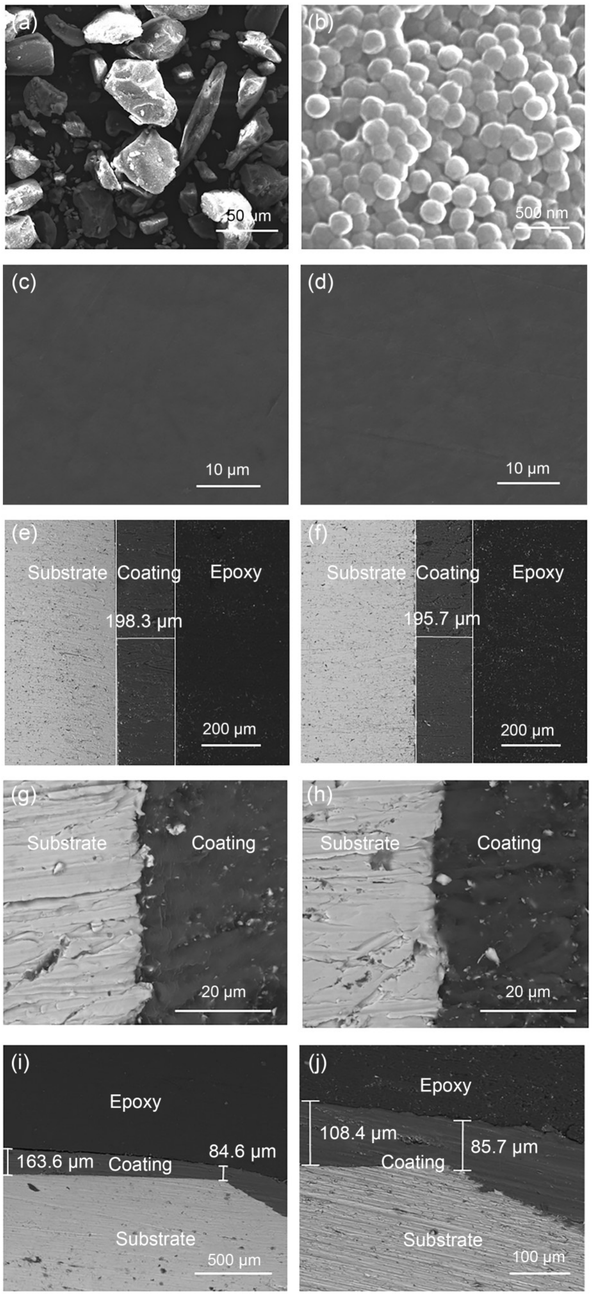

Fig. 7 SEM images of ECTFE powder and coating: (a and b) ECTFE powder; (c and d) outer surface of coating before and after soaking; (e and g) cross-sectional morphology of the coating center before soaking; (f and h) cross-sectional morphology of the coating center after soaking; (i and j) cross-sectional morphology of the coating edge before and after soaking

approximately 200 μm. After soaking, as shown in Figs. 7f and 7h, the cross-sectional morphology of the central coating remains intact and smooth, exhibiting no signs of cracking or delamination. This observation confirms that the protection performance against corrosion on the steel substrate center is still maintained at a high level. Fig. 7i is the edge cross-sectional morphology of the coated steel before soaking, revealing a gradual thinning of the coating edge with a minimum thickness of only 84.6 μm. This renders the coating edge vulnerable as it becomes the primary area for corrosive medium breakthrough. Fig. 7j shows the edge cross-sectional morphology of the coated steel after soaking, where no obvious changes are observed at the micron scale range, and no corrosive products and delamination phenomena are detected at the interface.

3.2 EDS analysis of coated steel during soaking

Fig. 8 shows the line scan of Fe, Cl, F, and O ions in the coating and substrate interface after different soaking periods. Based on the distribution of Fe and Cl, as well as the chemical composition analysis of both the coating and substrate, the interface between the coating and the steel substrate can be clearly distinguished. The Cl ion content and distribution remain unchanged during the soaking time. Fe ions diffuse to the coating side due to the ion diffusion caused by chemical reaction. F ions exhibit uniform distribution

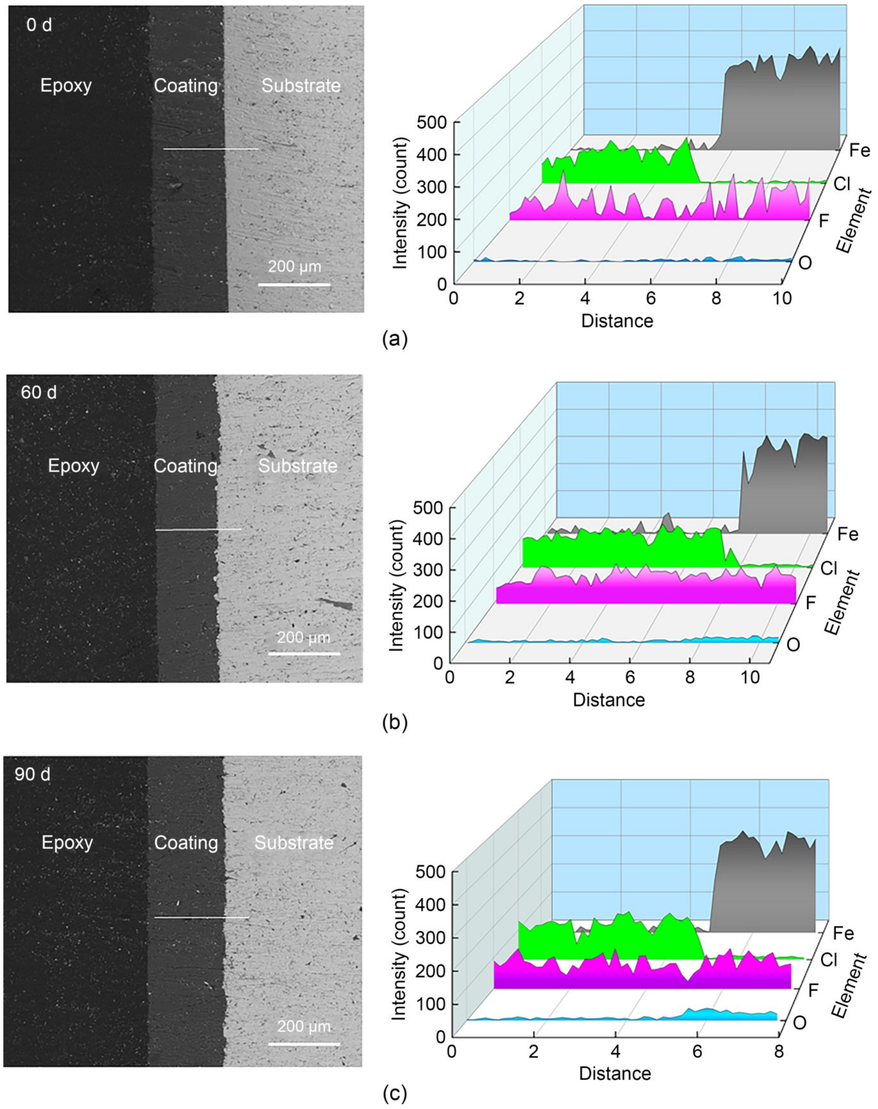

Fig. 8 Elemental line scan at the interface of the coated steel samples soaking for different periods: (a) 0 d; (b) 60 d; (c) 90 d. References to color refer to the online version of this figure

along the entire line scan before and after soaking, with negligible changes in the content. This is attributed to the relatively small radius of F, resulting in a limited dissociation and diffusion into the steel substrate during heat treatment, which facilitates the bonding between the coating and the steel substrate. The affinity between F and steel leads to preferential binding with Fe ions rather than sharing electrons with the C chain. Consequently, Fe ions can gradually permeate into the coating, serving as additional bonding between the coating and the steel matrix. In addition, the dissociated F disrupts the semi-crystalline structure, resulting in a weaker crystallinity at the interface compared to that on the surface in XRD. O ions are not inherent constituents of the coating and steel substrate; their presence is attributed solely to corrosion. Therefore, O content serves as a crucial indicator for characterizing the corrosion of the steel substrate. It should be noted that the unsoaked sample exhibits an extremely low level of O content. After soaking for 60 to 90 d, O content on the steel substrate gradually increases, indicating that a micro-zone corrosion reaction is occurring. This is a prelude to the pre-characteristics of macroscopic corrosion.

Fig. 9 shows the line scan of the steel substrate surface after coating removal at different soaking periods. The dashed-box section in Fig. 9a indicates the scan area, located at the edge of the coating with a sweeping direction from edge to center. As shown in Fig. 9b, the unsoaked steel substrate is flat and smooth, with uniform distribution of all tested elements along the scan line. O content is significantly low. After soaking for 60 d, as shown in Fig. 9c, the edge surface of the steel substrate appears uneven and eroded, indicating that corrosion has occurred. The gradual increase in contents of Cl and O ions and the decrease in those of Fe and F ions are attributed to the penetration of Cl ions from the solution into the steel substrate surface. When the soaking time exceeds 60 d, as shown in Figs. 9c and 9d, O content is higher at the edge and lower at the center, while Fe and F contents exhibit an

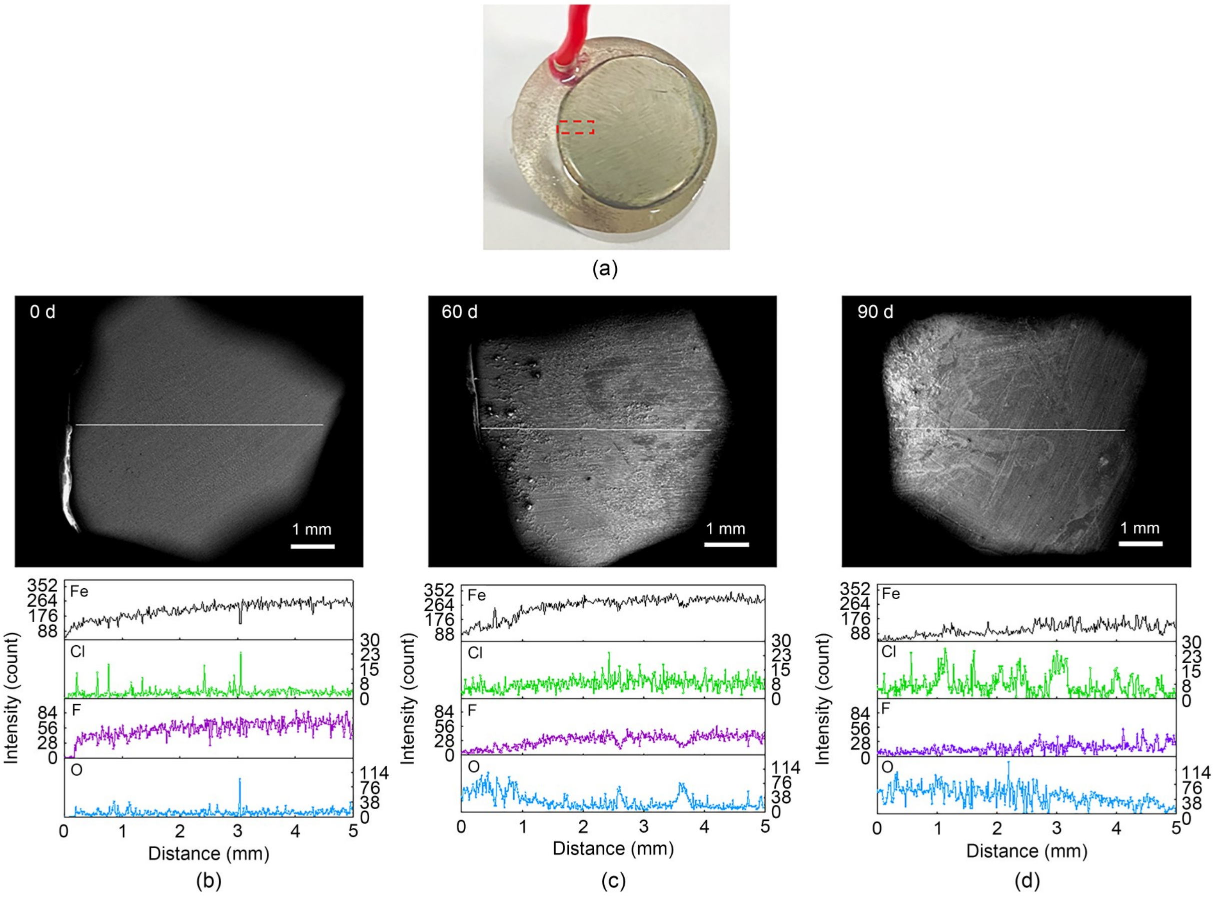

(a)

(b)

(c)

(d)

Fig. 9 Elemental line scan at the steel surface after removing coatings of the coated steel soaking at different periods: (a) scan area; (b) before soaking; (c) after soaking for 60 d; (d) after soaking for 90 d

opposite trend. This can be attributed to the thinner coating edge being more susceptible to penetration by the corrosive medium, leading to preferential corrosion initiation and subsequent increase in O content with a decrease in Fe and F contents. These initial corrosion products cannot be macroscopically detected through the coating and there is no obvious delamination at the interface in micro-scale. Only upon removing the coating can the corrosion traces be observed on the steel substrate surface, as shown in Figs. 9c and 9d.

3.3 Electrochemical corrosion and associated performance test analysis

3.3.1 Hydrophilic/hydrophobicity performance analysis

Fig. 10 shows the water contact angle test results of the ECTFE coating before and after soaking for 90 d. As shown in Fig. 10a, the initial water contact angle of the ECTFE coating is measured at 92.29°, indicating the intermediate level of water wettability on its surface. After soaking for 90 d, the water contact angle decreased to 86.51° and the coating surface exhibited a certain degree of hydrophilicity, as shown in Fig. 10b. This phenomenon may be attributed to the alterations in the micro- and nano-scale roughness of the coating surface caused by the penetration of the corrosive medium.

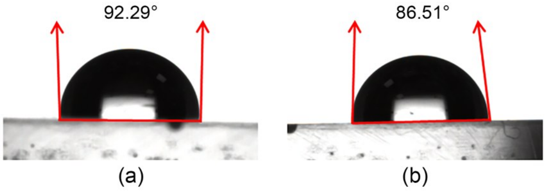

Fig. 10 Water contact angles of ECTFE coating before (a) and after (b) soaking for 90 d

3.3.2 Adhesion analysis

Before soaking, the adhesion of the ECTFE coating is classified as level 1, primarily due to residual stresses generated within the ECTFE during curing that create shear stresses at the interface between the coating and the steel substrate (Cai et al., 2021). Furthermore, F can diffuse into the steel substrate, promoting bonding between the coating and the steel substrate. After soaking for 90 d, the adhesion significantly decreased to level 5, indicating that the coating has essentially lost adhesion. This phenomenon may be attributed to the penetration of the corrosive medium and its expansion at the interface between the coating and the steel substrate.

3.3.3 EIS analysis

The EIS curves of bare steel and the coated steel soaking in 3.5% (mass fraction) NaCl solution at different periods are shown in Fig. 11. Fig. 11a is the Nyquist plot of bare steel, which exhibits an arc segment, indicating its lack of corrosion protection capability due to direct expose to the solution. The diameter of the impedance arc gradually decreases over time, indicating a continuous progression of the corrosion reaction. In Fig. 11c, the Bode plot of bare steel shows an impedance modulus at low frequency ($|Z|_{0.01\ \mathrm{Hz}}$) ranging from 10^2–10^3 $\Omega\cdot\mathrm{cm}^2$, with an overall decreasing trend within 90 d. Fig. 11e shows the phase angle plot of bare steel, which exhibits the maximum phase angle in the low and medium frequency regions, indicating that corrosion initiates immediately after the corrosive medium contacts with the substrate surface (Xiang et al., 2021).

Fig. 11b shows the Nyquist plot for coated steel. It exhibits a semicircular capacitance arc at low frequencies and a capacitance arc with a larger radius of curvature at high frequencies in the initial period, indicating two-time constants that suggest contact between the corrosive medium and the steel substrate resulting in a corrosion reaction after soaking for 1 d. This phenomenon is likely to arise from penetration from the thin part of the coating edge. The curvature radius of the capacitance arc in the low frequency region can serve as an indicator for evaluating the protective performance of the coating, while the capacitance arc in the high frequency region is attributed to charge transfer in the interface between the coating and substrate (Wang HH et al., 2021). The curvature radius of the capacitance arc gradually decreases with the soaking time in both high and low frequency regions, indicating a decrease in the protective performance of the coating and an increase in charge transfer at the interface. This is reflected by the changes in content and distribution of Fe, Cl, and O ions in the EDS line scan at the interface. Fig. 11d shows the Bode plot of the coated steel, wherein the impedance modulus of the coating at low frequency ($|Z|_{0.01\ \mathrm{Hz}}$) decreases from an initial 10^6 $\Omega\cdot\mathrm{cm}^2$ to 10^4 $\Omega\cdot\mathrm{cm}^2$ after 90 d, which is consistent with the decreasing trend of the curvature radius of the capacitance arc in the Nyquist plot. Compared with bare steel, the impedance modulus of the coating in

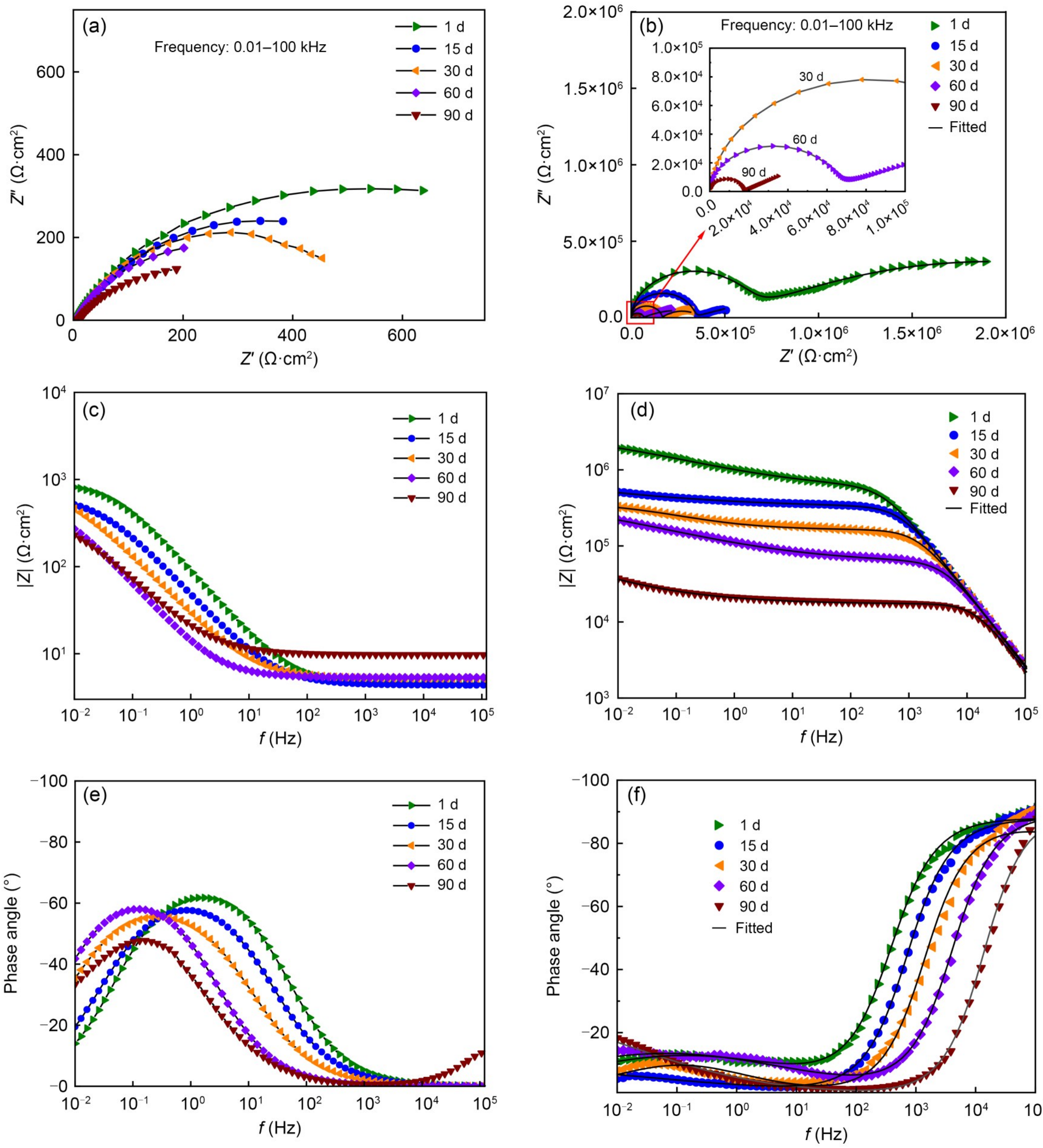

Fig. 11 Nyquist plot (a and b), Bode plot (c and d), and phase angle plot (e and f) of bare steel and the coated steel soaking in 3.5% (mass fraction) NaCl solution at different periods: (a, c, and e) bare steel; (b, d, and f) coated steel. *Z′* is the real part of the impedance; *Z″* is the imaginary part of the impedance

each period is at least two orders of magnitude higher, indicating superior protective performance of the coating. Fig. 11f shows the phase angle plot of the coated steel, which remains constant at high frequency, but shows a broad range of corrosion response peaks in the low and medium frequency regions, indicating two-time constant characteristics. This further suggests that the corrosive medium penetrates the steel substrate from the edge of the coating (Huttunen-Saarivirta et al., 2011; Yang et al., 2022).

Equivalent circuit diagrams were used to simulate EIS data for bare steel and coated steel. The equivalent circuits of bare steel and coated steel are shown in Figs. 12a and 12b, respectively. In the equivalent circuits, constant phase element (CPE) is used to simulate the capacitance C. R_s represents solution resistance; R_c characterizes the barrier performance of the coating (Wang HH et al., 2021); R_{ct} reflects the charge transfer resistance in the interfacial reaction; C_c is the coating capacitance; C_{dl} is the double-layer capacitance.

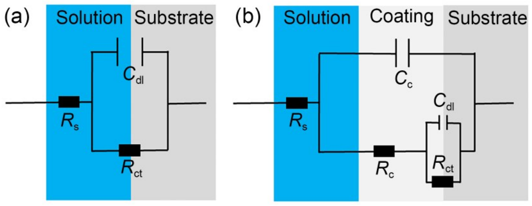

Fig. 12 Equivalent circuits of bare steel (a) and coated steel (b)

Tables 1 and 2 show the EIS fitting data of bare steel and coated steel, respectively. The overall error margin of fitting data is below 15%, with that for most of the bare steel even below 5%. As shown in Table 1, the bilayer resistance of bare steel is negligible due to immediate corrosion reaction upon direct contact with NaCl solution. In Table 2, the coating resistance reaches 5.62×10^5 Ω·cm^2 after soaking for 1 d and remains at a similar level over 30 d. After soaking for 90 d, the coating resistance decreases to 1.72×10^4 Ω·cm^2, due to a reduction in its crystalline state and significant weakening of the interfacial bond between the coating and steel substrate during long-term soaking. Consequently, the barrier properties of the coating are compromised and its resistance is diminished, leading to a weakened protective effect and intensified ion diffusion. Additionally, the charge transfer resistance is weakened, resulting in an overall decrease in R_{ct} and R_c (Liu et al., 2021).

Table 1 Electrochemical fitting parameters of the bare steel in Fig. 9

Time (d)	R_s (Ω·cm^2)	R_{ct} (Ω·cm^2)	C_{dl} (F/cm^2)
1	4.53	920.91	2.68×10^{-3}
15	5.17	880.21	9.94×10^{-3}
30	4.37	640.33	5.48×10^{-3}
60	5.33	580.06	2.19×10^{-2}
90	9.71	400.67	1.86×10^{-2}

Table 2 Electrochemical fitting parameters of the coated steel in Fig. 9

Time (d)	R_s (Ω·cm^2)	R_c (Ω·cm^2)	C_c (F/cm^2)	R_{ct} (Ω·cm^2)	C_{dl} (F/cm^2)
1	4.67	5.62×10^5	8.11×10^{-10}	2.72×10^6	9.54×10^{-7}
15	5.53	3.18×10^5	8.07×10^{-10}	2.17×10^6	8.93×10^{-6}
30	4.95	1.62×10^5	9.32×10^{-10}	2.20×10^5	8.24×10^{-6}
60	5.55	6.01×10^4	6.62×10^{-10}	3.97×10^5	9.16×10^{-6}
90	8.95	1.72×10^4	6.21×10^{-10}	1.40×10^4	1.26×10^{-4}

Water absorption will increase the dielectric constant of the coating, leading to an increase in the coating capacitance. Smaller coating capacitance (C_c) implies lower water absorption and superior corrosion resistance (Chang et al., 2021). Due to the intermediate hydrophilic-hydrophobic nature of the ECTFE coating surface, water absorption is impeded. C_c of the coating increases during 15 to 30 d, indicating that water is penetrating into the coating. During 30 to 60 d, C_c of the coating gradually decreases, due to the generation of corrosion products such as Fe^{2+} and Fe^{3+} during ion diffusion, which obstruct the penetration path and result in a decrease in the water absorption. During 60 to 90 d, C_c remains relatively stable, indicating that water absorption in the internal pores of the coating has reached a dynamic equilibrium. The double-layer capacitances (C_{dl}) of bare steel and coated steel gradually increase with the soaking time, suggesting that corrosion reactions are still ongoing.

3.3.4 Potential dynamic polarization curve analysis

Fig. 13 shows the open circuit potentials of bare steel and coated steel soaking in 3.5% (mass fraction) NaCl solution at different periods. The deviation in OCP

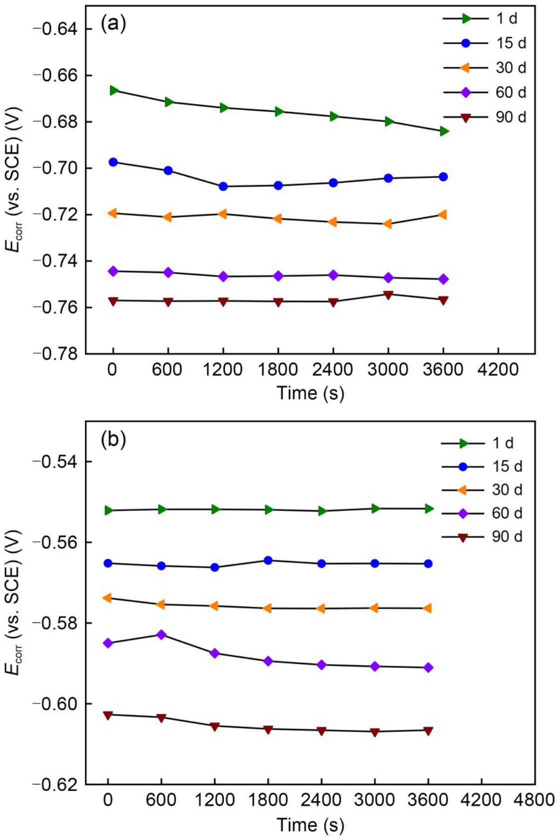

Fig. 13 OCP curves of bare steel (a) and coated steel (b) soaking in 3.5% (mass fraction) NaCl solution in different periods. E_{corr} is the corrosion potential

at 600 s for the sample soaking for 60 d may relate to the heterogeneous reactions due to the local non-uniform composition and structure of the outer layer of the ECTFE coating (Xu et al., 2022). The OCPs of both the bare steel and coated steel gradually decrease over time, with the former shifting from −0.67 V to −0.76 V within 90 d, and the latter from −0.55 V to −0.61 V. This indicates a gradual increase in the corrosion probability. Compared to bare steel, coated steel exhibits a higher OCP throughout the soaking period, indicating that the ECTFE coating can protect the substrate (Zhao et al., 2021). This is primarily attributed to the dense structure of ECTFE, which acts as a barrier against corrosive media penetration and restricts the formation of continuous corrosion products beneath the coating.

Fig. 14 shows the dynamic potential polarization curves of bare steel and the coated steel soaking in 3.5% (mass fraction) NaCl solution for different periods. The corrosion potentials (E_{corr}) and corrosion currents (i_{corr}) of the bare steel and coated steel were determined by fitting the Tafel extrapolation method, as listed in Table 3.

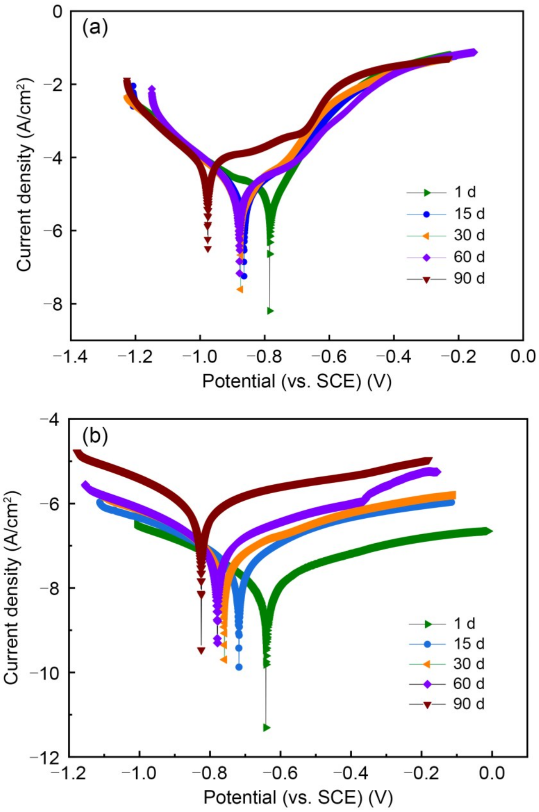

Fig. 14 Polarization curves of the bare steel (a) and coated steel (b) soaking in 3.5% (mass fraction) NaCl solution in different periods

Table 3 Electrochemical fitting parameters of the bare steel and coated steel

Time (d)	Bare steel		Coated steel	
	E_{corr} (vs. SCE) (V)	i_{corr} (A/cm^2)	E_{corr} (vs. SCE) (V)	i_{corr} (A/cm^2)
1	−0.78	5.32×10^{-5}	−0.64	2.19×10^{-8}
15	−0.86	4.32×10^{-5}	−0.71	6.35×10^{-8}
30	−0.87	4.96×10^{-5}	−0.75	8.70×10^{-8}
60	−0.88	4.44×10^{-5}	−0.77	1.72×10^{-7}
90	−0.97	1.61×10^{-4}	−0.82	1.13×10^{-6}

The corrosive protection efficiency (η_{p}) of the ECTFE coating was calculated using Eq. (1), as described in (Wan et al., 2021).

$$\eta_{\mathrm{p}}=\frac{i^{\mathrm{a}}_{\mathrm{corr}}-i^{\mathrm{b}}_{\mathrm{corr}}}{i^{\mathrm{a}}_{\mathrm{corr}}}\times100\%, \tag{1}$$

where $i^{\mathrm{a}}_{\mathrm{corr}}$ and $i^{\mathrm{b}}_{\mathrm{corr}}$ are the self-corrosion current densities of bare steel and coated steel, respectively. As shown in Table 3, the initial self-corrosion potential of bare steel is −0.78 V with a corresponding self-corrosion current density of 5.32×10^{-5} A/cm^2. These values remain relatively stable from 15 to 60 d, indicating that the corrosion rate of bare steel remains consistent during this period. After 90 d, the self-corrosion potential experiences a negative shift to −0.97 V and the self-corrosion current increases to 1.61×10^{-4} A/cm^2, indicating an elevation in corrosion rate.

The initial self-corrosion potential of the coated steel is −0.64 V, accompanied by a self-corrosion current density of 2.19×10^{-8} A/cm^2. After soaking for 90 d, the self-corrosion potential decreases to −0.82 V while the self-corrosion current density increases to 1.13×10^{-6} A/cm^2, with a coating protection rate of 99.29%. The self-corrosion current density of the coated steel is 2–3 orders of magnitude lower than that of bare steel in the whole soaking period, indicating a slow rate of corrosion. Furthermore, the self-corrosion current density of the ECTFE coating after 90 d is lower than that of atmospheric plasma spraying (APS) Cr_3C_2-25NiCr coating (8.001×10^{-6} A/cm^2 after 30 d) (Zavareh et al., 2016), Zn-Cu-Ti coating (4.32×10^{-6} A/cm^2 after 60 d) (Zhang et al., 2022), and high-velocity oxygen fuel (HVOF) sprayed Cr_3C_2-NiCr coating (5.61×10^{-5} A/cm^2 after 70 d) (Wang KL et al., 2021). The high level of protection from the coating indicates that it still maintains its protective capabilities even in the presence of edge corrosion.

3.4 Neutral salt spray test analysis

Fig. 15 shows the macroscopic morphological changes of the coated steel with cross scratches in the neutral salt spray environment for 720 h, with the sample edges sealed with a thick epoxy coating. As shown in Fig. 15, yellow corrosion products emerged in the scratch area after 120 h, and gradually intensified over time due to the accumulation of yellow $Fe_2O_3 \cdot H_2O$. In addition, corrosion can also be observed at the edge of the coating due to the weak resistance to corrosion caused by the thinness. For the scratch area where the macroscopic corrosion phenomenon predominantly occurs, longitudinal direction is the primary mode of corrosion while lateral development is somewhat inhibited. It is evident that the initial adhesion between coating and steel substrate and the semi-crystalline structure confer a significant capability of corrosion protection upon the coating, thereby affording long-term effective protection to the substrate.

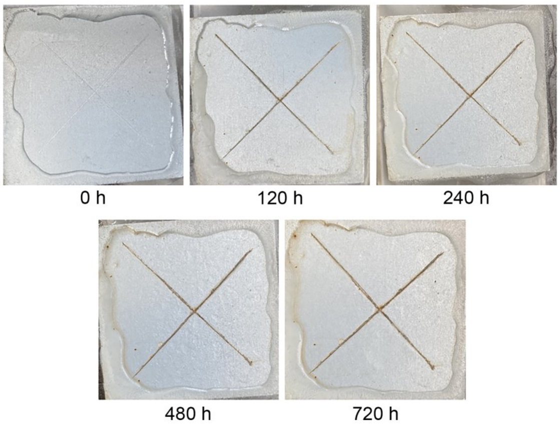

Fig. 15 Salt spray test results after exposing the scratched coatings to salt spray for 720 h. References to color refer to the online version of this figure

5 Conclusions

In this study, ECTFE coating approximately 200 μm thick was prepared on the surface of carbon steel by electrostatic spraying and heat treatment at 260 °C. The edge corrosion behavior of ECTFE-coated steel and its mechanism were thoroughly investigated, leading to the following conclusions:

1. The outer surface structure of the ECTFE coating remains essentially unaltered before and after soaking in 3.5% (mass fraction) NaCl solution for 90 d.

2. F ions can diffuse into the steel substrate, which enhances the bonding between the coating and steel substrate but weakens the crystalline structure.

3. Due to the edge thickness of the coating, corrosive media can easily penetrate from the edges and cause corrosion.

4. Despite edge corrosion, the coated steel exhibits great corrosive protection performance, due to its dense and stable structure with excellent barrier properties.

Acknowledgments

This work is supported by the Zhejiang Postdoctoral Merit-Based Funding (No. ZJ2020030), the China Postdoctoral Science Foundation (No. 2020M681920), and the Zhejiang Sci-Tech University Youth Innovation Program (No. 2021Q038), China.

Author contributions

Minjia WANG designed the research. Peihu SHEN and Jun WEN finished the experiments. Minjia WANG and Peihu SHEN processed the corresponding data. Peihu SHEN wrote the first draft of the manuscript. Biqin DONG and Hedong LI helped to organize the manuscript and revised the first draft. Peihu SHEN and Minjia WANG revised further and edited the final version.

Conflict of interest

Peihu SHEN, Jun WEN, Biqin DONG, Hedong LI, and Minjia WANG declare that they have no conflict of interest.

References

Abdel-Hady EE, El-Toony MM, 2015. Grafting of vinyl pyrrolidone/styrene onto ethylene/chlorotrifluoroethylene membrane for proton exchange membrane fuel cell. *Electrochimica Acta*, 176:472-479.
https://doi.org/10.1016/j.electacta.2015.06.136

Alibakhshi E, Akbarian M, Ramezanzadeh M, et al., 2018. Evaluation of the corrosion protection performance of mild steel coated with hybrid sol-gel silane coating in 3.5 wt.% NaCl solution. *Progress in Organic Coatings*, 123:190-200.
https://doi.org/10.1016/j.porgcoat.2018.07.008

Cai GY, Xiao S, Deng CM, et al., 2021. CeO_2 grafted carbon nanotube via polydopamine wrapping to enhance corrosion barrier of polyurethane coating. *Corrosion Science*, 178:109014.
https://doi.org/10.1016/j.corsci.2020.109014

Chang XT, Chen XQ, Zhang QY, et al., 2021. Alumina nanoparticles-reinforced graphene-containing waterborne polyurethane coating for enhancing corrosion and wear resistance. *Corrosion Communications*, 4:1-11.
https://doi.org/10.1016/j.corcom.2021.11.004

Cui ZL, Drioli E, Lee YM, 2014. Recent progress in fluoropolymers for membranes. *Progress in Polymer Science*, 39(1): 164-198.

https://doi.org/10.1016/j.progpolymsci.2013.07.008

Douche D, Elmsellem H, Anouar EH, et al., 2020. Anti-corrosion performance of 8-hydroxyquinoline derivatives for mild steel in acidic medium: gravimetric, electrochemical, DFT and molecular dynamics simulation investigations. *Journal of Molecular Liquids*, 308:113042. https://doi.org/10.1016/j.molliq.2020.113042

Ghanbari A, Bordbar-Khiabani A, Warchomicka F, et al., 2023. PEO/polymer hybrid coatings on magnesium alloy to improve biodegradation and biocompatibility properties. *Surfaces and Interfaces*, 36:102495. https://doi.org/10.1016/j.surfin.2022.102495

Giannetti E, 2005. Thermal stability and bond dissociation energy of fluorinated polymers: a critical evaluation. *Journal of Fluorine Chemistry*, 126(4):623-630. https://doi.org/10.1016/j.jfluchem.2005.01.008

Haeri Z, Ramezanzadeh B, Ramezanzadeh M, 2022. Recent progress on the metal-organic frameworks decorated graphene oxide (MOFs-GO) nano-building application for epoxy coating mechanical-thermal/flame-retardant and anticorrosion features improvement. *Progress in Organic Coatings*, 163:106645. https://doi.org/10.1016/j.porgcoat.2021.106645

Hsissou R, Benzidia B, Hajjaji N, et al., 2018. Elaboration and electrochemical studies of the coating behavior of a new nanofunctional epoxy polymer on E24 steel in 3.5% NaCl. *Portugaliae Electrochimica Acta*, 36(4):259-270. https://doi.org/10.4152/pea.201804259

Hsissou R, Benhiba F, Echihi S, et al., 2021. Performance of curing epoxy resin as potential anticorrosive coating for carbon steel in 3.5% NaCl medium: combining experimental and computational approaches. *Chemical Physics Letters*, 783:139081. https://doi.org/10.1016/j.cplett.2021.139081

Hsissou R, Azogagh M, Benhiba F, et al., 2022a. Insight of development of two cured epoxy polymer composite coatings as highly protective efficiency for carbon steel in sodium chloride solution: DFT, RDF, FFV and MD approaches. *Journal of Molecular Liquids*, 360:119406. https://doi.org/10.1016/j.molliq.2022.119406

Hsissou R, Benhiba F, El Aboubi M, et al., 2022b. Synthesis and performance of two ecofriendly epoxy resins as a highly efficient corrosion inhibition for carbon steel in 1 M HCl solution: DFT, RDF, FFV and MD approaches. *Chemical Physics Letters*, 806:139995. https://doi.org/10.1016/j.cplett.2022.139995

Huttunen-Saarivirta E, Yudin VE, Myagkova LA, et al., 2011. Corrosion protection of galvanized steel by polyimide coatings: EIS and SEM investigations. *Progress in Organic Coatings*, 72(3):269-278. https://doi.org/10.1016/j.porgcoat.2011.04.015

Kajánek D, Hadzima B, Buhagiar J, et al., 2019. Corrosion degradation of AZ31 magnesium alloy coated by plasma electrolytic oxidation. *Transportation Research Procedia*, 40:51-58. https://doi.org/10.1016/j.trpro.2019.07.010

Lei HB, He DL, Guo YN, et al., 2018. Synthesis and characterization of UV-absorbing fluorine-silicone acrylic resin polymer. *Applied Surface Science*, 442:71-77. https://doi.org/10.1016/j.apsusc.2018.02.134

Liu CB, Qian B, Hou PM, et al., 2021. Stimulus responsive zeolitic imidazolate framework to achieve corrosion sensing and active protecting in polymeric coatings. *ACS Applied Materials & Interfaces*, 13(3):4429-4441. https://dx.doi.org/10.1021/acsami.0c22642

Liu G, Pan J, Xu XL, et al., 2020. Preparation of ECTFE porous membrane with a green diluent TOTM and performance in VMD process. *Journal of Membrane Science*, 612:118375. https://doi.org/10.1016/j.memsci.2020.118375

MOHURD (Ministry of Housing and Urban-Rural Development of the People's Republic of China), 2009. Corrosion of Metals and Alloys-Electrochemical Test Methods–Guidelines for Conducting Potentiostatic and Potentiodynamic Polarization Measurements, GB/T 24196–2009. National Standards of the People's Republic of China (in Chinese).

MOHURD (Ministry of Housing and Urban-Rural Development of the People's Republic of China), 2021. Paints and Varnishes–Cross-Cut Test, GB/T 9286–2021. National Standards of the People's Republic of China (in Chinese).

Molhi A, Hsissou R, Damej M, et al., 2021. Contribution to the corrosion inhibition of C38 steel in 1 M hydrochloric acid medium by a new epoxy resin PGEPPP. *International Journal of Corrosion and Scale Inhibition*, 10(1):399-418. https://doi.org/10.17675/2305-6894-2021-10-1-23

Pan J, Ma WY, Huang LL, et al., 2021. Fabrication and characterization of ECTFE hollow fiber membranes via low-temperature thermally induced phase separation (L-TIPS). *Journal of Membrane Science*, 634:119429. https://doi.org/10.1016/j.memsci.2021.119429

Rudnev VS, Vaganov-Vil'kins AA, Yarovaya TP, et al., 2016. Polytetrafluoroethylene-oxide coatings on aluminum alloys. *Surface and Coatings Technology*, 307:1249-1254. https://doi.org/10.1016/j.surfcoat.2016.07.035

Sengupta S, Murmu M, Mandal S, et al., 2021. Competitive corrosion inhibition performance of alkyl/acyl substituted 2-(2-hydroxybenzylideneamino) phenol protecting mild steel used in adverse acidic medium: a dual approach analysis using FMOs/molecular dynamics simulation corroborated experimental findings. *Colloids and Surfaces A: Physicochemical and Engineering Aspects*, 617:126314. https://doi.org/10.1016/j.colsurfa.2021.126314

Shen GZ, Zhang LY, Wu W, et al., 2022. Design and fabrication of enhanced corrosion-resistant LDH-Zn-G/Ni dual-layer structural coatings on magnesium alloys. *Journal of Alloys and Compounds*, 917:165475. https://doi.org/10.1016/j.jallcom.2022.165475

Simone S, Figoli A, Santoro S, et al., 2012. Preparation and characterization of ECTFE solvent resistant membranes and their application in pervaporation of toluene/water mixtures. *Separation and Purification Technology*, 90:147-161. https://doi.org/10.1016/j.seppur.2012.02.022

Singh L, Devgan K, Samra KS, 2012. Effect of swift heavy ion irradiation on ethylene–chlorotrifluoroethylene copolymer. *Radiation Physics and Chemistry*, 81(11):1741-1746. https://doi.org/10.1016/j.radphyschem.2012.06.006

Steffi AP, Balaji R, Chen SM, et al., 2021. Rational construction of $SiO_2/MoS_2/TiO_2$ composite nanostructures for antibiofouling and anti-corrosion applications. *ChemistrySelect*, 6(5):917-927.
https://doi.org/10.1002/slct.202004263

Steffi AP, Balaji R, Chandrasekar N, et al., 2022a. High-performance anti-corrosive coatings based on rGO-SiO_2-TiO_2 ternary heterojunction nanocomposites for superior protection for mild steel specimens. *Diamond and Related Materials*, 125:108968.
https://doi.org/10.1016/j.diamond.2022.108968

Steffi AP, Balaji R, Prakash N, et al., 2022b. Incorporation of SiO_2 functionalized gC_3N_4 sheets with TiO_2 nanoparticles to enhance the anticorrosion performance of metal specimens in aggressive Cl^- environment. *Chemosphere*, 290: 133332.
https://doi.org/10.1016/j.chemosphere.2021.133332

Wan S, Chen HK, Ma XZ, et al., 2021. Anticorrosive reinforcement of waterborne epoxy coating on Q235 steel using NZ/BNNS nanocomposites. *Progress in Organic Coatings*, 159:106410.
https://doi.org/10.1016/j.porgcoat.2021.106410

Wang H, Xu JH, Du XS, et al., 2021. A self-healing polyurethane-based composite coating with high strength and anticorrosion properties for metal protection. *Composites Part B: Engineering*, 225:109273.
https://doi.org/10.1016/j.compositesb.2021.109273

Wang HH, Duan YH, Ma XT, et al., 2021. Polyisocyanate bridged environmental graphene/epoxy nanocomposite coatings with excellent anticorrosion performance. *Progress in Organic Coatings*, 153:106167.
https://doi.org/10.1016/j.porgcoat.2021.106167

Wang KL, Hong S, Wei Z, et al., 2021. Long-term corrosion behavior of HVOF sprayed Cr_3C_2-NiCr coatings in sulfide-containing 3.5 wt.% NaCl solution. *Journal of Materials Research and Technology*, 15:3122-3132.
https://doi.org/10.1016/j.jmrt.2021.09.131

Xiang YX, He Y, Tang WW, et al., 2021. Fabrication of robust Ni-based TiO_2 composite@TTOS superhydrophobic coating for wear resistance and anti-corrosion. *Colloids and Surfaces A: Physicochemical and Engineering Aspects*, 629: 127394.
https://doi.org/10.1016/j.colsurfa.2021.127394

Xu LY, Fu XJ, Su HJ, et al., 2022. Corrosion and tribocorrosion protection of AZ31B Mg alloy by a hydrothermally treated PEO/chitosan composite coating. *Progress in Organic Coatings*, 170:107002.
https://doi.org/10.1016/j.porgcoat.2022.107002

Yan ST, Tang P, Ling ZW, et al., 2022. An analytical investigation of the collapse of asymmetrically corroded pipes under external pressure. *Journal of Zhejiang University-SCIENCE A (Applied Physics & Engineering)*, 23(5):358-374.
https://doi.org/10.1631/jzus.A2100487

Yang SH, Fang H, Li H, et al., 2022. Synthesis of tung oil-based vinyl ester resin and its application for anti-corrosion coatings. *Progress in Organic Coatings*, 170:106967.
https://doi.org/10.1016/j.porgcoat.2022.106967

Yao N, Chau J, Elele E, et al., 2017. Characterization of microporous ECTFE membrane after exposure to different liquid media and radiation. *Journal of Membrane Science*, 532: 89-104.
https://doi.org/10.1016/j.memsci.2017.03.007

Zavareh MA, Sarhan AADM, Zavareh PA, et al., 2016. Electrochemical corrosion behavior of carbon steel pipes coated with a protective ceramic layer using plasma and HVOF thermal spray techniques for oil and gas. *Ceramics International*, 42(2):3397-3406.
https://doi.org/10.1016/j.ceramint.2015.10.134

Zhang WY, Zhang T, Zhu ZX, et al., 2022. Corrosion electrochemistry properties of thermally sprayed Zn-Cu-Ti coating in simulated ocean atmosphere. *Journal of Materials Research and Technology*, 21:3235-3247.
https://doi.org/10.1016/j.jmrt.2022.10.108

Zhang ZQ, Li YL, Zhu XY, et al., 2021. Meso-scale corrosion expansion cracking of ribbed reinforced concrete based on a 3D random aggregate model. *Journal of Zhejiang University-SCIENCE A (Applied Physics & Engineering)*, 22(11):924-940.
https://doi.org/10.1631/jzus.A2100304

Zhao HR, Ding JH, Liu PL, et al., 2021. Boron nitride-epoxy inverse “nacre-like” nanocomposite coatings with superior anticorrosion performance. *Corrosion Science*, 183:109333.
https://doi.org/10.1016/j.corsci.2021.109333